Hindawi
Advances in Civil Engineering
Volume 2018, Article ID 9589364, 13 pages
https://doi.org/10.1155/2018/9589364

Research Article

Study on the Fractal Characteristics of Fracture Network Evolution Induced by Mining

Tao Liang,[1] Xiaoli Liu,[1] Sijing Wang,[1,2] Enzhi Wang,[1] and Quansheng Li[3]

[1]*State Key Laboratory of Hydro-Science and Engineering, Tsinghua University, Beijing 100084, China*
[2]*Institute of Geology and Geophysics of the Chinese Academy of Sciences, Beijing 100029, China*
[3]*State Key Laboratory of Water Resources Protection and Utilization in Coal Mining, Shenhua Group Co., Ltd., Beijing 100011, China*

Correspondence should be addressed to Xiaoli Liu; xiaoli.liu@tsinghua.edu.cn

Received 16 January 2018; Revised 8 April 2018; Accepted 30 April 2018; Published 20 June 2018

Academic Editor: Dingwen Zhang

The evolution and distribution of fracture network induced by mining is essential to determine the mechanical properties and permeability of disturbed rock mass. In this paper, the similar material model tests are employed to simulate the stress variation, cyclic breaking, and fracture formation and distribution status of the overlying strata with different loading conditions, rock properties, and mining process. The fractal dimension of mining-induced fracture network varied with mining advancing, and the evolvement laws of fracture network with mining advancing and different mining advancing footage are concerned and obtained. By establishing the relationship between the fractal dimension and the mining length in different horizontal and vertical zones, it demonstrates that the fractal dimensions in horizontal and vertical zones have a self-similar characteristic, and the distribution of the fractal dimension of the mining-induced fractures shows generally the "W"-type trend.

1. Introduction

The original equilibrium state of the underground rock is disturbed by mining, and the fracture network in the overlying rock mass gradually forms and evolves with the rock stress redistribution. The mechanism of the fracturing and evolution of mining-induced cracks plays a great important role on the permeability assessment, overburden strata subsidence prediction, and the security and stability evaluation of mining rock mass [1–6]. According to Yu et al. [2], it is probably one of the most important issues in mining science to recognize and describe quantitatively the evolution of fracture network resulting from mining processes, on which many researchers have carried out fruitful research in recently years. Qian and Xu [7] proposed the two-stage development law of mining-induced cracks and revealed the "O"-shape distribution characteristics in a long-wall face of a coal mine. Li et al. [8] discussed the effect of key strata on the distribution of fractures and concluded that an elliptic paraboloid zone would be formed in the overlying strata due to the connection of the rock mass breaking induced fractures and the strata layers separation induced fractures in mining process. Li et al. [9] described the distribution characteristics of roof separation fractures in the process of fully mechanized top coal caving and derived the equivalent areas of bed-separated cracks before and after the key strata breaking and the permeability coefficients in different crack districts.

The fractal geometry proposed by Mandelbrot [10] is a powerful tool to quantitatively describe complex objects and phenomenon of irregular. In recent years, increasing attention has been focused on the combined application of fractal theory and physical models, by which considerable progress has been made in quantitative description of the evolution law of mining-induced fractures [11–20].

In the process of coal mining, the authors put forward underground reservoirs construction technology in mined out area, which is a new idea on coal-water coordinate mining, for comprehensive utilization of underground water

Table 1: Site stratigraphy and physical properties.

Strata number	Lithology	Strata thickness (m)	Initial permeability coefficient (m/d)	In situ vertical stress (MPa)	Strata density (kg/m^3)
1	Aeolian sand and loess	30	0.5–5.0		2000
2	Mudstone	15	0.0002	34.86	2304
3	Medium coarse-grained sandstone	5	0.02	50.00	2550
4	Mudstone	20	0.0002	25.22	2204
5	Fine sandstone-siltstone	10	0.004	5.26	2133
6	Mudstone	15	0.0002	25.22	2204
7	Number 2 coal seam	5	0.0001	14.49	1306
8	Mudstone	15	0.0002	34.86	2304
9	Fine sandstone-siltstone	20	0.004	5.26	2133
10	Mudstone	15	0.0002	34.86	2304
11	Medium coarse-grained sandstone	20	0.02	50.00	2550
12	Mudstone	20	0.0002	25.22	2204
13	Fine sandstone-siltstone	10	0.004	5.26	2133
14	Mudstone	10	0.0002	25.22	2204
15	Medium coarse-grained sandstone	20	0.02	50.00	2550
16	Mudstone	20	0.0002	25.22	2204
17	Medium coarse-grained sandstone	20	0.004	5.26	2133
18	Number 5 coal seam	5	0.0001	19.54	1295
19	Mudstone	15	0.0002	34.86	2304
20	Medium coarse-grained sandstone	15	0.02	50.00	2550
21	Mudstone	10	0.009	34.86	2304
22	Medium coarse-grained sandstone	10	0.02	50.00	2550

resources, protection of aquifer, safe production of coal mines, and underground water reuse. This technology is meaningful for sustainable development of underground resources, including coal mine resources, especially in arid and semiarid areas, where the water resources are very short. The distribution and evolution of mining-induced fractures in the overlying and floor rock mass play an important role in determining the location and capacity of the underground reservoir and in groundwater operation and purification as well. In this study, the Daliuta coal mine in the Ordos Basin of northeastern China, where underground reservoirs were constructed, is taken as the engineering background. Fracture network evolution and distribution induced by mining is essential to determine the mechanical properties and permeability of disturbed rock mass. In this paper, the physical similarity model was made and by which the deformation and collapse of the overlying rock mass were well observed and recorded under different conditions. By analyzing the fractal dimension variation of fracture networks of different working conditions and different zones with the mining face advancing, the distribution and evolvement laws of fracture network with mining speed and in different horizontal and vertical zones are concerned, which provides a basis for studying the relationship between cracks evolution and corresponding permeability change of mining rock mass.

2. Experimental Procedure

2.1. Geological Conditions. According to the geological investigation, the representative stratigraphic distribution in the Daliuta mine field and the physical properties are presented in Table 1.

Table 2: Similarity ratios.

Similarity coefficient	Similarity ratio
C_{ω_a}	1/10
C_γ, C_μ, C_ε, C_φ, C_R	1
C_k, C_t	10
C_L, C_δ, C_c, C_σ, C_{σ_t}, C_{σ_c}, C_E	100

γ: bulk density; L: length; δ: displacement; ε: strain; E: elastic modulus; σ: stress; σ_t: tensile strength; σ_c: compressive strength; c: cohesion; φ: internal friction angle; μ: Poisson's ratio; k: permeability coefficient; R: softening coefficient; ω_a: water absorption; t: time duration.

2.2. Similarity Theory and Similar Materials. Similar simulation study is an important means for scientific research, during which a model with artificial materials is made in the laboratory according to the similar principles and with a certain scale. With the aid of test instruments, the physical and mechanical parameters and distribution rules in the model are observed and obtained, from which the mechanical phenomenon and law of rock-pressure distribution of the prototype are inferred, and hereby to solve the practical problems in rock engineering.

Similar material and prototype used in the fluid-solid coupling model test should satisfy (1) and (2) simultaneously [21, 22]:

$$K_x\frac{\partial^2 p}{\partial x^2} + K_y\frac{\partial^2 p}{\partial y^2} + K_z\frac{\partial^2 p}{\partial z^2} = S\frac{\partial p}{\partial t} + \frac{\partial e}{\partial t} + W, \quad (1)$$

where K_x, K_y, and K_z are the permeability coefficients in x, y, and z directions, respectively; p is the water pressure; S is the water storage coefficient; e is the volumetric strain; and W is the source and sink.

Table 3: Physical and mechanical parameters of the prototype and the model.

Number	Parameters	Prototype	Model
1	Bulk density (kN/m^3)	21.0~25.5	21.0~25.5
2	Compressive strength (MPa)	5~50	0.05~0.5
3	Permeability coefficient (cm/s)	1×10^{-4}~1×10^{-3}	1×10^{-5}~1×10^{-4}
4	Softening coefficient	Greater than 0.75	Greater than 0.75
5	Water absorption	0.2%~0.5%	2%~5%

Table 4: Similar material parameters.

Number	Simulated rock stratum	Bulk density (kg/m^3)	Compressive strength (MPa)	Permeability coefficient (cm/s)	Softening coefficient	Water absorption
1	Mudstone	2300	0.35	$7.2E-5$	0.88	0.02
2	Medium coarse-grained sandstone	2550	0.50	$9.0E-5$	0.81	0.03
3	Mudstone	2200	0.25	$1.0E-4$	0.78	0.03
4	Fine sandstone-siltstone	2100	0.05	$9.0E-5$	0.75	0.03

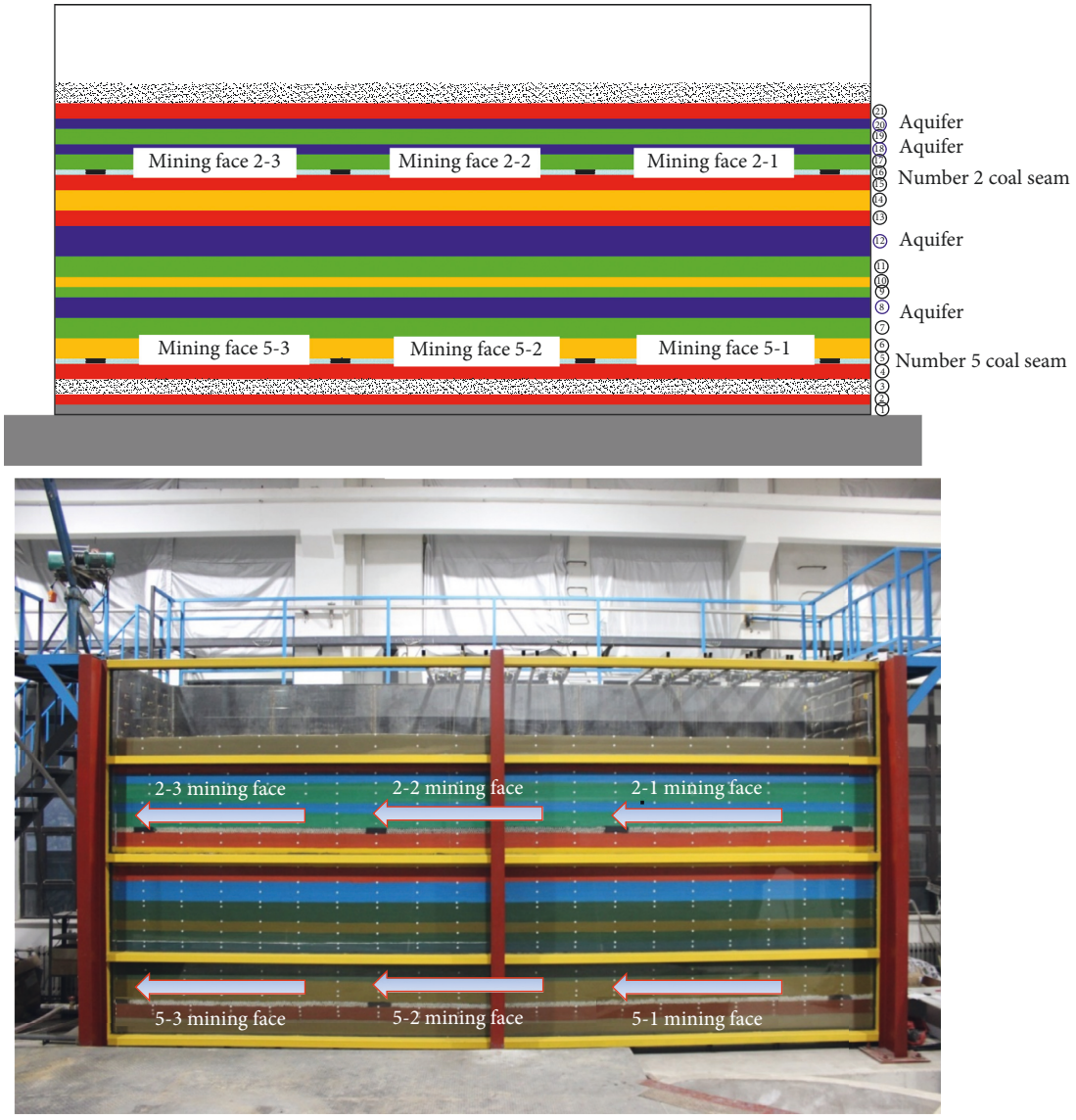

Figure 1: Cross section of the physical simulation model.

Table 5: Description of the mining process (mining face 5-3).

Mining length (mm)	Caving height (mm)	Caving length (mm)	Caving description
300	50	300	Immediate roof falls
500	50	200	Immediate roof falls
600	50	100	Immediate roof falls
700	50	100	Immediate roof falls
800	50	100	Immediate roof fall
850	100	800	Main roof collapses (integral)
900	50	100	Immediate roof falls
950	50	50	Immediate roof falls
1100	100	300	Main roof collapses (partial)
1150	50	50	Immediate roof falls
1200	200	1200	Main roof collapses (integral)
1250	50	50	Immediate roof falls
1350	100	100	Immediate roof falls
1400	50	50	Immediate roof falls
1450	200	250	Main roof collapses (partial)
1500	300	500	Main roof collapses (partial)
1550	50	100	Immediate roof falls
1650	100	200	Main roof collapses (partial)
1750	50	100	Immediate roof falls
1800	600	1800	Main roof collapses (integral)
1850	50	50	Immediate roof falls
1900	50	50	Immediate roof falls
1950	50	50	Immediate roof falls
2100	50	150	Immediate roof falls

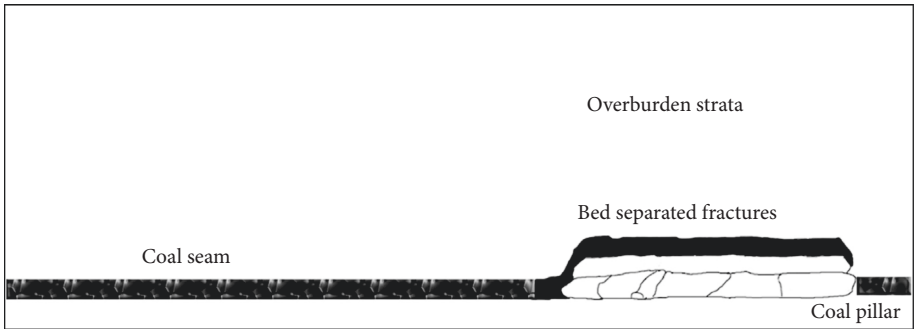

(a)

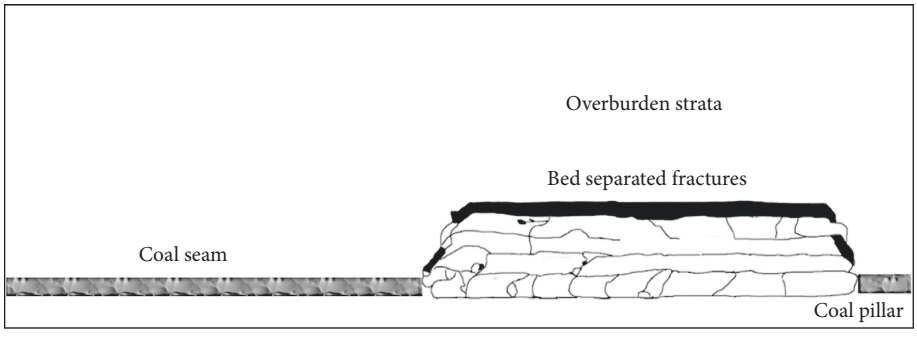

(b)

Figure 2: Continued.

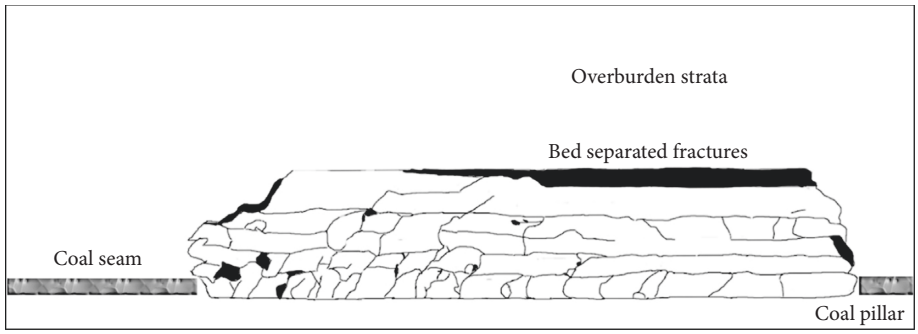

(c)

Figure 2: Fracture network diagrams (mining face 5-3). Mining length: (a)850 mm; (b)1200 mm; (c)1800 mm.

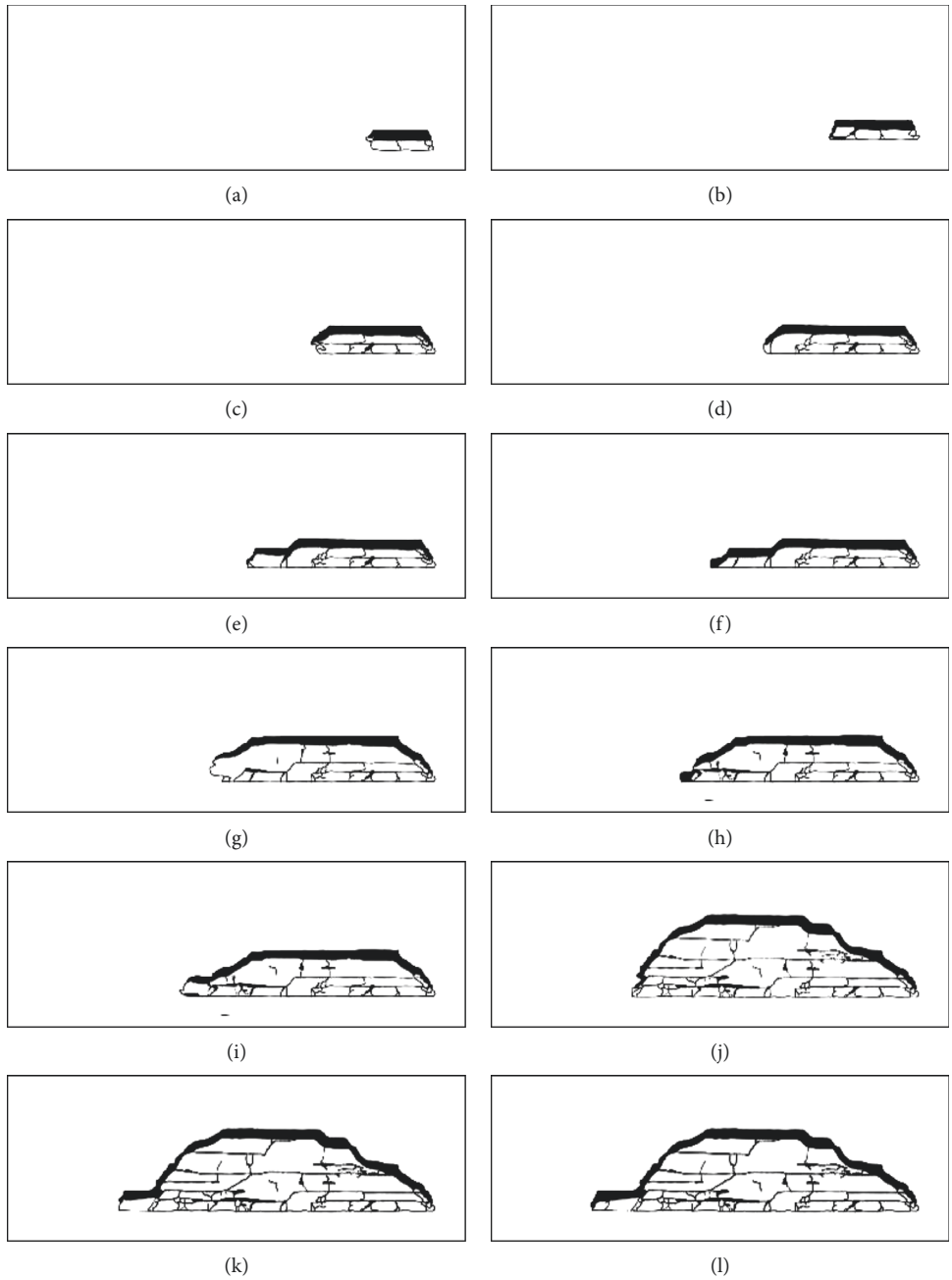

(a) (b)

(c) (d)

(e) (f)

(g) (h)

(i) (j)

(k) (l)

Figure 3: Continued.

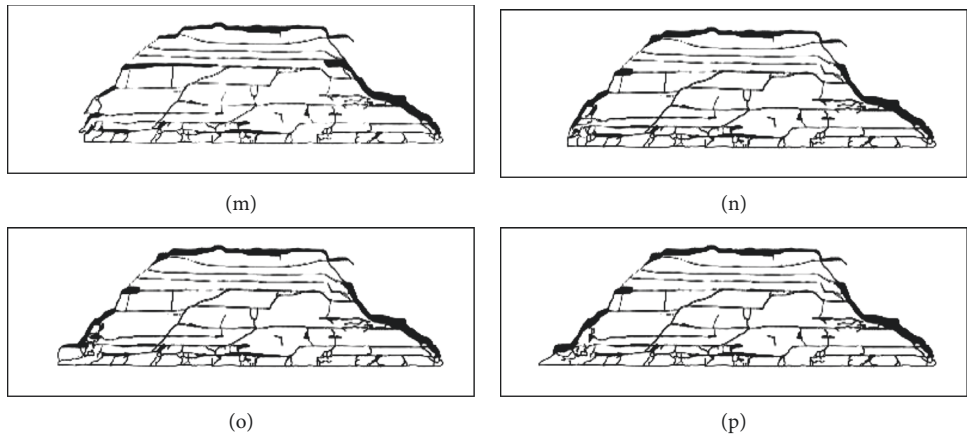

(m) (n)

(o) (p)

Figure 3: Fracture network evolution (mining face 5-1). Mining length: (a) 300 mm; (b) 450 mm; (c) 600 mm; (d) 800 mm; (e) 1000 mm; (f) 1100 mm; (g) 1200 mm; (h) 1250 mm; (i) 1350 mm; (j) 1500 mm; (k) 1700 mm; (l) 1800 mm; (m) 1900 mm; (n) 1950 mm; (o) 2050 mm; (p) 2100 mm.

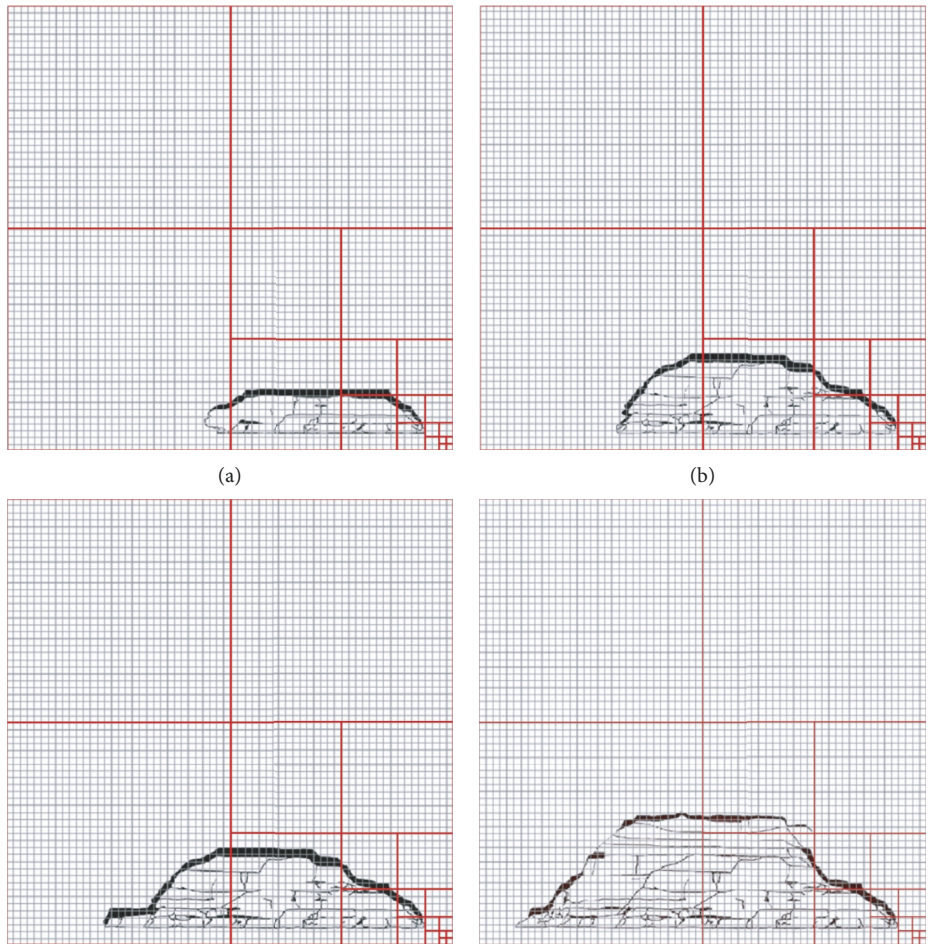

(a) (b)

(c) (d)

Figure 4: Schematic diagram for the "counting the boxes" method. Mining face 5-1 at a mining length of (a) 1200 mm; (b) 1500 mm; (c) 1800 mm; (d) 2100 mm.

Table 6: List for calculating D_f (mining face 5-1 at a mining length of 1200 mm).

r	1	2	4	8	16	32	64	128
N	24509	7071	2130	711	249	92	34	14
$\ln(1/r)$	0	−0.69	−1.39	−2.08	−2.77	−3.47	−4.16	−4.85
$\ln N$	10.11	8.86	7.66	6.57	5.52	4.52	3.53	2.64

Table 7: List for calculating D_f (mining face 5-1 at a mining length of 1500 mm).

r	1	2	4	8	16	32	64	128
N	38677	11458	3750	1350	510	180	63	21
$\ln(1/r)$	0	−0.69	−1.39	−2.08	−2.77	−3.47	−4.16	−4.85
$\ln N$	10.56	9.35	8.23	7.21	6.23	5.19	4.14	3.04

Table 8: List for calculating D_f (mining face 5-1 at a mining length of 1800 mm).

r	1	2	4	8	16	32	64	128
N	49959	14383	4579	1599	578	190	66	22
$\ln(1/r)$	0	−0.69	−1.39	−2.08	−2.77	−3.47	−4.16	−4.85
$\ln N$	10.82	9.57	8.43	7.38	6.36	5.25	4.19	3.09

Table 9: List for calculating D_f (mining face 5-1 at a mining length of 2100 mm).

r	1	2	4	8	16	32	64	128
N	59485	18261	6243	2320	910	316	104	34
$\ln(1/r)$	0	−0.69	−1.39	−2.08	−2.77	−3.47	−4.16	−4.85
$\ln N$	10.99	9.81	8.74	7.75	6.81	5.76	4.64	3.53

$$G\nabla^2 u + (\lambda + G)\frac{\partial e}{\partial x} + X + p\frac{\partial \alpha}{\partial x} + \alpha\frac{\partial p}{\partial x} = \rho\frac{\partial^2 u}{\partial t^2},$$

$$G\nabla^2 v + (\lambda + G)\frac{\partial e}{\partial y} + Y + p\frac{\partial \alpha}{\partial y} + \alpha\frac{\partial p}{\partial y} = \rho\frac{\partial^2 v}{\partial t^2}, \quad (2)$$

$$G\nabla^2 \omega + (\lambda + G)\frac{\partial e}{\partial z} + Z + p\frac{\partial \alpha}{\partial z} + \alpha\frac{\partial p}{\partial z} = \rho\frac{\partial^2 \omega}{\partial t^2},$$

where $\nabla^2 = (\partial^2/\partial x^2) + (\partial^2/\partial y^2) + (\partial^2/\partial z^2)$ is the Laplace operator; $G = (E/2(1+\mu))$ is the shear modulus; $\lambda = (\mu E/((1+\mu)(1-2\mu)))$ is the lame constant; $e = (\partial u/\partial x) + (\partial v/\partial y) + (\partial \omega/\partial z)$ is the volume strain; E is the modulus of elasticity; μ is Poisson's ratio; u, v, and ω are the displacements in the directions x, y, and z, respectively; X, Y, and Z are the volume forces in the directions x, y, and z, respectively; α is the effective stress coefficient; ρ is the density; p is the water pressure.

Equations (1) and (2) are the basic equations of the fluid-solid coupling theory. The archetype and the model need to satisfy the above equations. Based on the similarity theory [23], the similarity coefficients of the similar model tests are derived to satisfy the following equations:

$$C_G\frac{C_u}{C_l^2} = C_\lambda\frac{C_e}{C_l} = C_G\frac{C_e}{C_l} = C_\gamma = C_p\frac{C_\alpha}{C_l} = C_\alpha\frac{C_p}{C_l} = C_\rho\frac{C_u}{C_t^2}, \quad (3)$$

$$C_k\frac{C_p}{C_l^2} = C_S\frac{C_p}{C_t} = \frac{C_e}{C_t} = C_W, \quad (4)$$

where C is the similarity coefficient. $C_G = G'/G''$, $C_\rho = \rho'/\rho''$, and so on, where the lower foot mark represents the physical variables or parameters that it represents, $'$ represents the prototype, and $''$ represents the model.

The model test should be based on the similarity principles, the hydrologic and geological conditions of the prototype, and the specific requirements of the research problems. At the same time, the similarity index and similarity ratio should be determined according to the conditions mentioned above as well as the field conditions of the model test. The similar materials were tested by adjusting the composition and proportion of similar materials and then determined through experimental verification. The main concerns of this model test are the deformation, failure, and permeability change of the overlying rock, so the main parameters of the similar model test are the bulk density, compressive strength (or tensile strength), and permeability coefficient. At the same time, because of the effect of groundwater, the softening coefficient and water absorption also need to satisfy a certain similarity with the prototype.

According to the principles of the similarity model test, the geometrical size, boundary condition, load and movement conditions of the model, and physical and mechanical parameters (e.g. bulk density, strength, deformation characteristics, and water characteristics) of the similar materials are similar to that of the prototype. Based on the elastic mechanics, the dimensional analysis method combined with the fluid-solid coupling theory; the values of the similar parameters are detailed in Table 2.

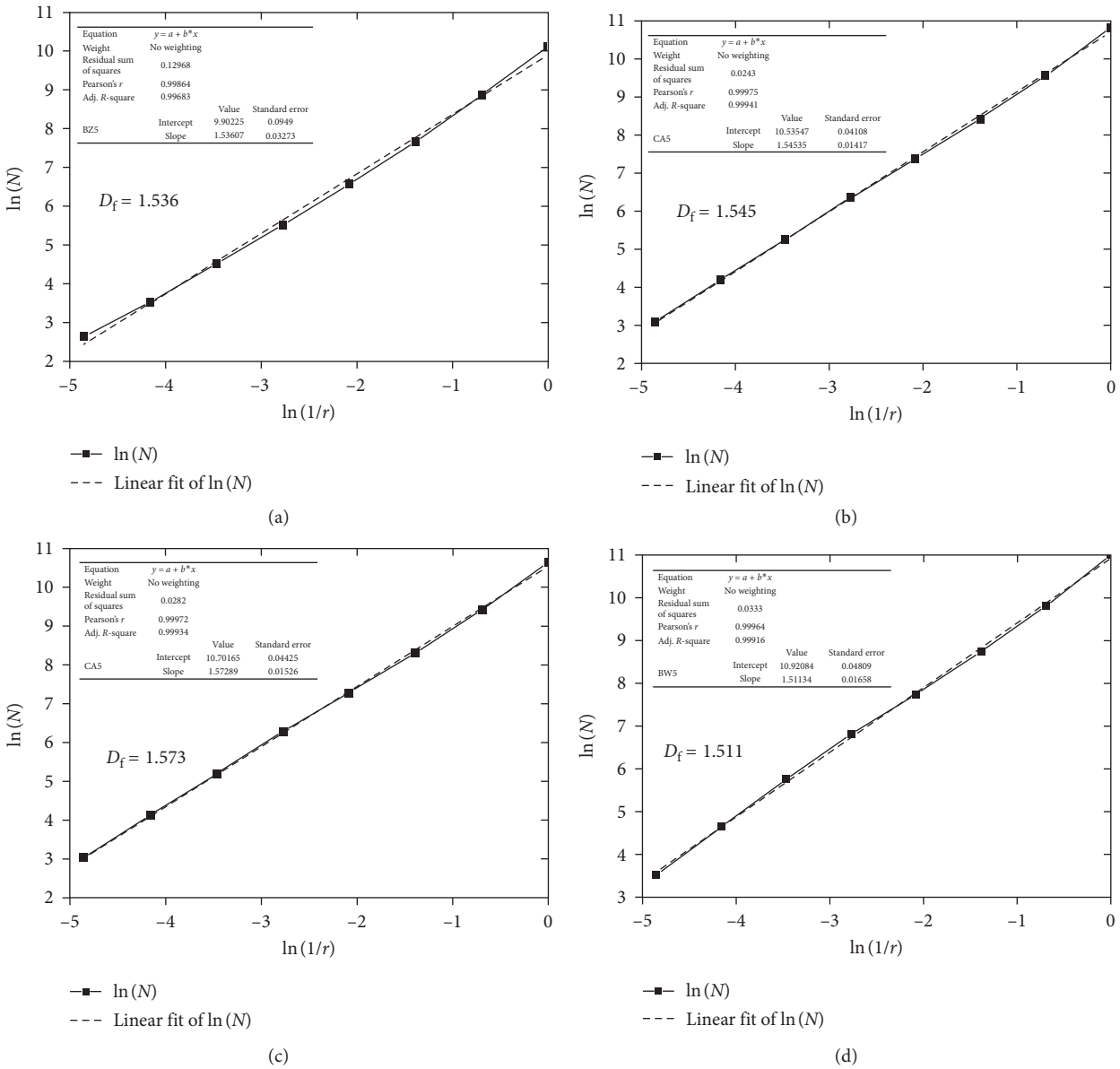

Figure 5: Schematic diagram for calculating D_f. Mining face 5-1 at a mining length of (a) 1200 mm; (b) 1500 mm; (c) 1800 mm; (d) 2100 mm.

The range of the physical and mechanical parameters of the similar materials in the model test is described in Table 3.

Based on the materials developed in [24], after many times of proportioning tests, similar materials meeting the test requirements are made, and the similar material parameters are listed in detail in Table 4.

2.3. Similarity Physical Model. The experiment is carried out in a large-scale model test bed designed by the authors, which is 8000 mm long, 1800 mm wide, and 4000 mm high, with the outer frame composed of I steel and channel steel and positive for toughened glass. There are open channels with the sealing cover on the elevation of coal seams on the back plate, used to simulate coal seam excavation, and inlet and outlet holes and flow control table on both sides of the test bed.

As shown in Figure 1, there are 21 similar material layers in the test bed from the bottom to the top, with a total height of 3000 mm, including the number 2 and number 5 similar coal seams with 50 mm thickness located on the elevation of 2250 mm and 500 mm, respectively. The similar pillar is 300 mm wide, by which each similar coal seam is separated in 3 mining faces with a length of 2100 mm. With different mining speeds, the coal seam in a different mining face is mined and the overburden strata movement, and the spatial distribution and evolution process of mining-induced fractures are observed and studied.

A real-time in situ monitoring program was carried out during and after the mining process. The items of monitoring include the stress in overburden strata and coal pillar, the displacement of overburden strata, and the water pressure in aquifer. A total of 160 sensors (e.g., displacement

meter, rock-pressure gauge, and water-pressure gauge) are arranged in the model, from which the data acquisition processing system feedback to the control terminal and the real-time curve will be obtained. Meanwhile, with the aid of total station instrument, 3D laser scanner, and high-speed digital camera, the displacement of 486 monitoring points distributed on the surface of the model is obtained as well.

3. Evolution of Mining-Induced Fracture Network

3.1. Simulation of the Mining Process. With the aid of the physical similarity model, the deformation and collapse of the overlying rock mass can be observed directly during the mining process. Taking the mining face 5-3, for example, the immediate roof falls with a width of 300 mm and height of 50 mm at the mining length of 300 mm. From 300 mm to 800 mm of the mining length, the immediate roof falls four times at an average width of 100 mm and height of 50 mm. Then, the main roof collapses with a height of 100 mm when the mining face advances 850 mm. During the next mining process, the integral caving of the main roof occurs at the mining length of 1200 mm and 1800 mm, accompanying periodical fall of the immediate roof at an average length of 50 mm to 150 mm and several partial collapses of the main roof. With the advancement in mining process, the fractures generate and propagate in the overlying rock strata. At the end of the mining process, the fracture network evolutes within the whole mined out area with a caving height of 600 mm. The description of the mining process in detail is presented in Table 5, and representative fracture network diagrams are shown in Figure 2.

3.2. Calculation of Fractal Dimension. In order to quantitatively analyse the expansion of fractures in mining rock masses, real-time video recording is performed in the process of the model test. Through the observation section in front of the physical model, the whole process of fracture generation, expansion, evolution, and strata failure during mining is well recorded. With the help of digital processing technology, the fracture network diagrams at different mining lengths are digitized (as shown in Figure 3). In this study, the calculation of fractal dimension is done by the method of "counting the boxes." Each diagram is extended to a square area with a length of integer power times of 2. The fracture network with a unit length size of box is covered, and the number of boxes needed to cover the network is counted. The size of the box is enlarged by 2 times, the calculation of the number of boxes required to cover the fracture network is repeated, and so on (as shown in Figure 4). For each fracture network, a set of data corresponding to box length r and the number of boxes N is obtained in this way. If the fracture network has a fractal character, the size of the box r and the number of boxes $N(r)$ will follow the relationship as shown in the following equation:

$$N(r) = r^{-D_f}, \tag{5}$$

where D_f is the fractal dimension. By drawing the relationship between $N(r)$ and $1/r$ in the double logarithmic coordinates, a straight line will be obtained, of which the slope is equal to D_f. Taking the mining face 5-1 at the mining lengths of 1200 mm, 1500 mm, 1800 mm, and 2100 mm, for example, N and r of the covering boxes for calculating the fractal dimension are listed in Tables 6–9. By drawing the relationship between $N(r)$ and $1/r$ in the double logarithmic coordinates, the slope of the straight line equal to D_f is obtained (as shown in Figure 5).

From (5) and the fractal dimension calculation process, we can see that for each fracture network, the fractal dimension reflects the density of fractures in the unit area, and the increase in the fractal dimension indicates the expanding of fractures and the increasing of the fractures density. By analyzing the fractal dimension variation of fracture diagrams of different working conditions and different zones at different mining lengths, we can quantitatively analyse the fracture expansion and evolution laws.

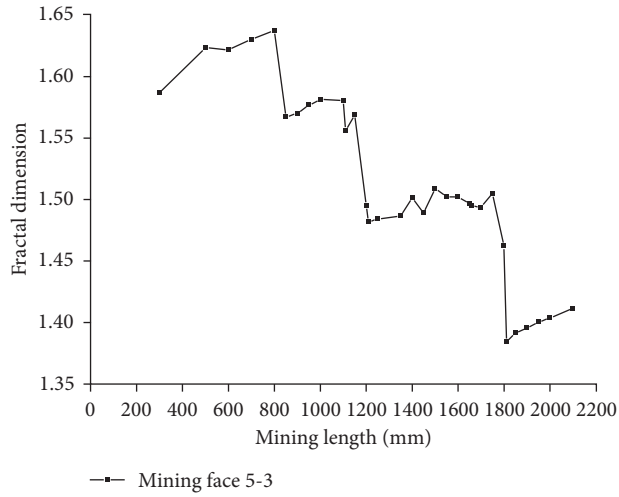

Figure 6: Evolution of the fractal dimension of fracture network with mining length.

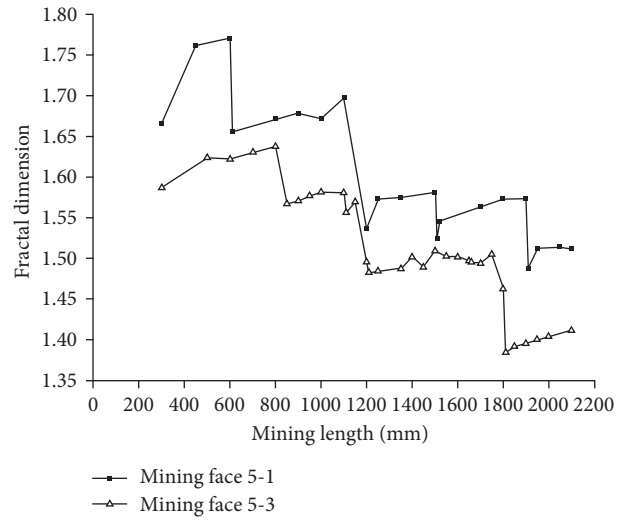

Figure 7: Relationship between the fractal dimension and mining length with different mining footage.

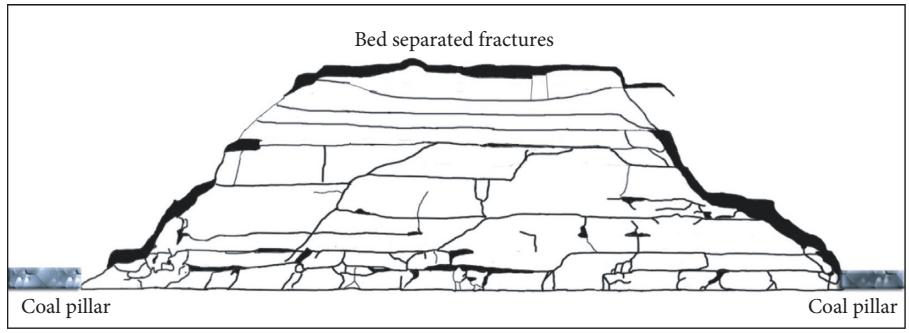

(a)

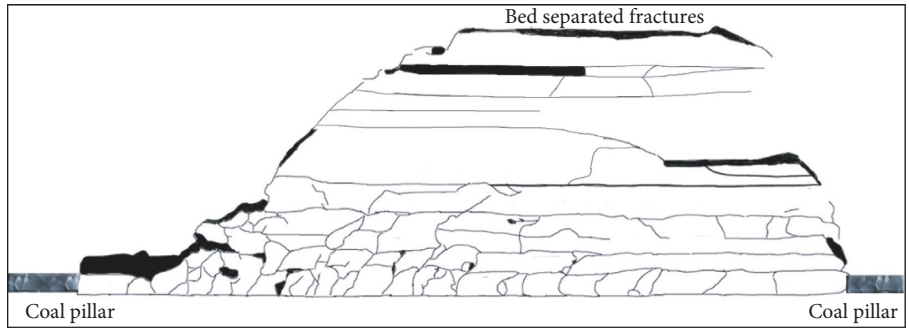

(b)

Figure 8: Fracture networks at the end of the mining process. Mining face: (a) 5-1; (b) 5-3.

Table 10: Horizontal zone description.

Zone number	H1	H2	H3	H4	H5	H6	H7
Mining length(mm)	0–300	300–600	600–900	900–1200	1200–1500	1500–1800	1800–2100

3.3. Fractal Dimension Evolution of Fracture Networks with Mining Process. The evolution of the fractal dimension of fracture networks with mining length is shown in Figure 6, by which the following features can be obtained:

(1) The curve can be separated in several stage-type folding lines, containing increasing segment and descending segment.

(2) The descending point corresponds exactly to the mining length, at which the main roof collapses (as shown in Table 5).

(3) Every point in the linear increasing segment corresponds to the mining length, at which the immediate roof falls (as shown in Table 5).

(4) The increasing segment can be fitted to a straight line, which means the regression relation between the fractal dimension D and the mining length L can be given by the following equation:

$$D = a * L + b, \tag{6}$$

where a and b are the parameters determined by the hydrogeological conditions, rock mechanical parameters, mining method, and so on.

Table 11: Vertical zone description.

Zone number	Zone height(mm)
V1	0–100
V2	100–200
V3	200–300
V4	300–400
V5	400–500
V6	500–600

3.4. Evolution of Fractal Dimension with Different Mining Footage. In order to analyse the influence of mining speed on the damage of overlying strata and the evolution of fracture propagation, mining faces 5-1 and 5-3 are mined with different mining advance footage. The relationship between the fractal dimension and mining length with different mining footage is shown in Figure 7, by which we can see that the mining face 5-1 (with a faster mining speed) has a larger fractal dimension than the mining face 5-3. Both the mining faces have the similar stage-type of the fractal dimension curve. Nevertheless, the 5-3 mining face has more points in increasing segment of the fractal dimension curve, which means having the shorter weighting interval in the immediate roof and a more developed fracture network in the caving zone, which can also be concluded from the

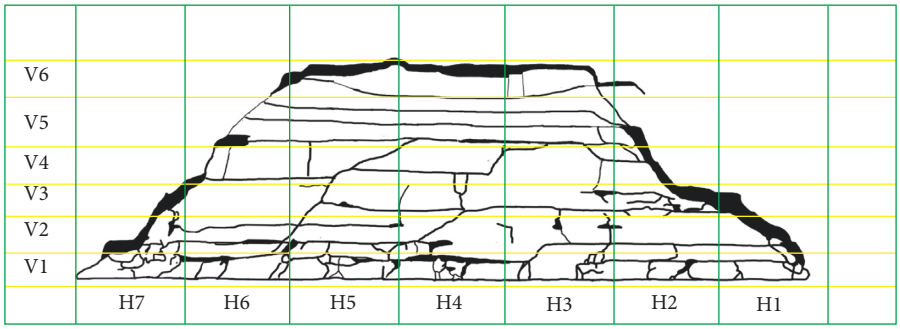

Figure 9: Schematic diagram for the fracture zones.

fracture network at the end of the mining process (as shown in Figure 8).

3.5. Evolution of Fractal Dimension in Different Caving Zones. With the advancing of mining face, how the fractures generate and develop in different horizontal and vertical zones is an aspect deserving to pay more attention on in this study. Based on this concern, 7 horizontal zones and 6 vertical zones are separated in mining face 5-1 (as shown in Tables 10 and 11 and Figure 9); the fractal dimension is calculated, respectively, and the fractal dimension curves are shown in Figures 10–13. The key findings are as follows:

(1) Figure 10 describes the evolution of the fractal dimension in horizontal zones with the mining face advancing. The evolution curves indicate that the fractal dimension in horizontal zones has a similar trend with the fractal dimension on the whole, that is, gradually increasing in general and reduces when the main roof collapses. The main reason may be that the collapse of the main roof gives rise to the closure of fractures in the caving zone.

(2) Figures 10 and 11 show that the fractal dimension at different mining progresses (such as 90 m, 120 m, 150 m, and 190 m) decreases with the increase of mining footage. On the whole, at the end of the mining process, the horizontal zone H3 and zone H6 have a relatively low fractal dimension, and the zones H1, H4, and H7, on the contrary, have a relatively high fractal dimension. The distribution of the fractal dimension of the fractures shows generally the "W"-type trend.

(3) Through the analysis of the fractal characteristics of the fracture networks of the working face and combining the district partition of the fractured rock mass after mining [15], it is found that the fractal dimension of the fractured rock mass near the cutting area decreases gradually with the increase of mining footage, which indicates that the fractures in the area are gradually compressed and closed, which is called the re-compressed area. The fractal dimension of fractured rock mass near the mining face area increases, which indicates that the fractures are gradually developed and expanded with the increase of mining footage, which is called the separation zone. With the increase of mining footage, the separation area away from the mining face is gradually transformed into a re-compressed area and the re-compressed area is gradually transformed into a stable area so that the fractal dimension of the horizontal zones of the fractured rock mass in the goaf is in dynamic changing.

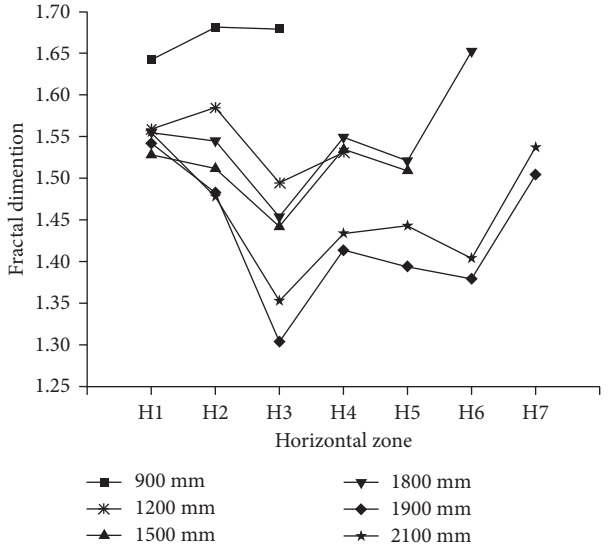

Figure 10: Evolution of the fractal dimension of crack network in different horizontal zones.

(4) Figure 12 shows the similar developing pattern of fractal dimension in vertical zones with that in horizontal zones. At the same time, it may be concluded by Figure 13 that, in general, the fractal dimensions reduce with the increase of the caving height; that is, the caving zone has a more developed fracture network than the fractured zone. Meanwhile, however, it should be pointed out that there is an exception sometimes in the transition zone between the fractured zone and sinking zone, due to the formation of the strata-separated fractures, which contribute much to the increase of the fractal dimension.

4. Conclusions

The fractal dimension is a very good tool to describe the evolution of mining-induced fractures network and its

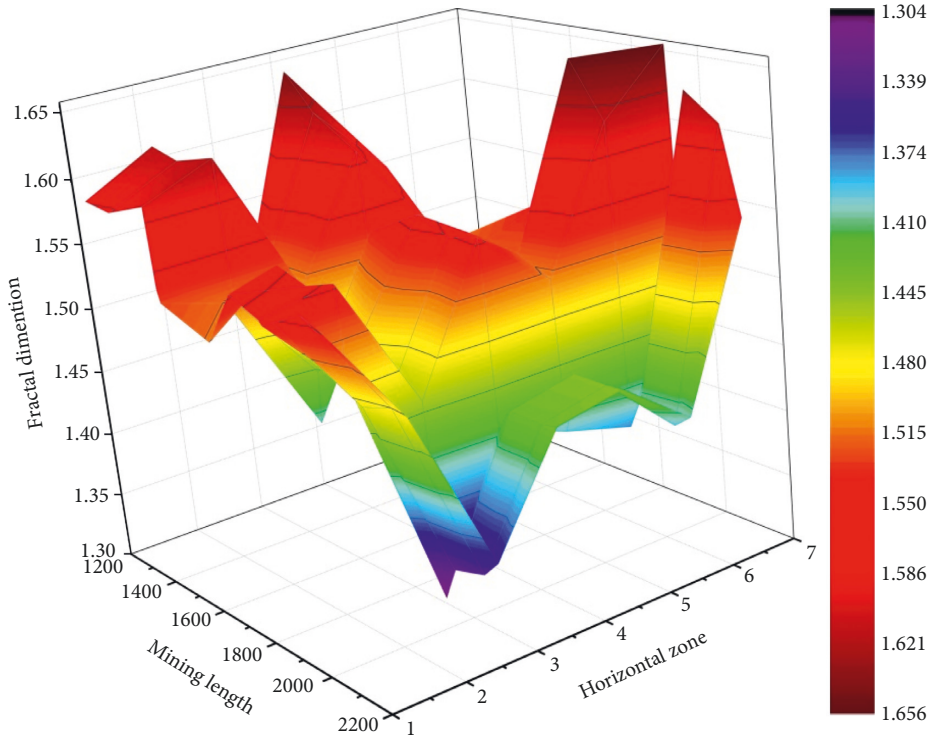

Figure 11: 3D colour map surface of evolution of the fractal dimension of crack network with mining length in different horizontal zones.

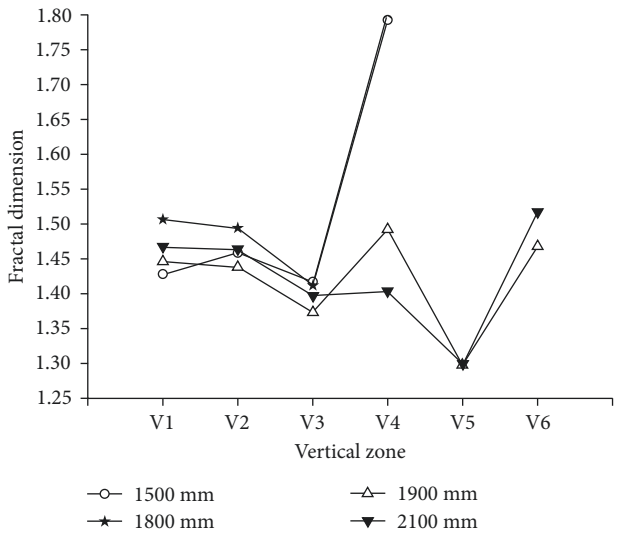

Figure 12: Evolution of the fractal dimension of crack network in different vertical zones.

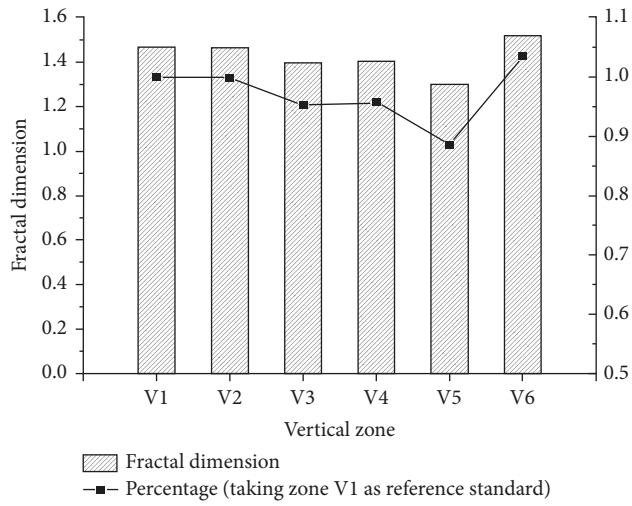

Figure 13: Ratio of the fractal dimension of crack network in different vertical zones.

evolution. In this paper, the fractal characteristics of fractures network induced by mining are studied in detail, and the following conclusions can be drawn:

(1) The evolution curves of the fractal dimension with mining length can be separated into several stage-type folding lines, containing increasing segment and descending segment. The descending point corresponds exactly to the mining length, at which the main roof collapses. The increasing segment can be described by linear relationship.

(2) The mining face with a faster mining speed has a larger fractal dimension. Nevertheless, the opposite of that has a shorter weighting interval in immediate roof and a more developed fracture networks in the caving zone.

(3) The fractal dimensions in horizontal and vertical zones have a self-similar characteristic, that is, gradually increasing in general and reduces when the main roof collapses, similar to the features on the whole.

(4) At the end of the mining process, the spatial distribution of mining-induced cracks may be saddle shaped.

(5) Generally, the fractal dimension reduces with the increase of the caving height, while in the transition zone between the fractured zone and sinking zone, on the contrary, the fractal dimensions increase because of the separation of strata layers.

Data Availability

The data used to support the findings of this study are available from the corresponding author upon request.

Conflicts of Interest

The authors declare that they have no conflicts of interest.

Acknowledgments

The authors would like to acknowledge the support by the National Natural Science Foundation-Outstanding Youth Foundation (Grant no. 51522903), the National Key Research and Development Plan (Grant no. 2016YFC0501104), the National Natural Science Foundation of China (Grant nos. 51479094 and 41772246), and the Open Research Fund Program of the State Key Laboratory of Hydroscience and Engineering (Grant nos. 2016-KY-02 and 2016-KY-05).

References

[1] T. Q. Liu, "Influence of mining activities on mine rock mass and control engineering," *Journal of China Coal Society*, vol. 20, pp. 1–5, 1995.

[2] G. M. Yu, H. P. Xie, H. W. Zhou, Y. Z. Zhang, and L. Yang, "Distribution law of cracks in structured rock mass and its experimental investigation," *Journal of Experimental Mechanics*, vol. 13, pp. 145–154, 1998.

[3] H. P. Xie, G. M. Yu, L. Yang, and Y. Z. Zhang, "Research on the fractal effects of crack network in overburden rock stratum," *Chinese Journal of Rock Mechanics and Engineering*, vol. 18, no. 2, pp. 147–151, 1999.

[4] O. Bour, P. Davy, C. Darcel et al., "A statistical scaling model for fracture network geometry, with validation on a multiscale mapping of a joint network (Hornelen Basin, Norway)," *Journal of Geophysical Research: Solid Earth*, vol. 107, no. B6, pp. 347–383, 2002.

[5] J. Weiss, "Scaling of fracture and faulting of ice on earth," *Surveys in Geophysics*, vol. 24, no. 2, pp. 185–227, 2003.

[6] P. A. Dowd, C. Xu, K. V. Mardia, and R. J. Fowell, "A comparison of methods for the stochastic simulation of rock fractures," *Mathematical Geology*, vol. 39, no. 7, pp. 697–714, 2007.

[7] M. G. Qian and J. L. Xu, "Study on the "O-shape" circle distribution characteristics of mining-induced fractures in the overlaying strata," *Journal of China Coal Society*, vol. 23, no. 5, pp. 466–469, 1998.

[8] S. G. Li, M. G. Qian, and P. W. Shi, "Study on the dynamic distribution characteristic of fissures elliptic paraboloid zone in the mining overlying strata," *Mine Pressure and Roof Management*, no. 3–4, pp. 44–46, 1999.

[9] S. G. Li, M. G. Qian, and P. W. Shi, "Study on bed-separated fissures of overlying stratum and interstice permeability in fully-mechanized top coal caving," *Chinese Journal of Rock Mechanics and Engineering*, vol. 19, no. 5, pp. 604–607, 2000.

[10] B. B. Mandelbrot, *The Fractal Geometry of Nature*, W. H. Freeman, San Francisco, CA, USA, 1982.

[11] T. Hirata, "Fractal dimension of fault systems in Japan: fractal structure in rock fracture geometry at various scales," *Pure and Applied Geophysics*, vol. 131, no. 1-2, pp. 157–170, 1989.

[12] T. Villemin, J. Angelier, and C. Sunwoo, "Fractal distribution of fault length and offsets: implications of brittle deformation evaluation—The Lorraine Coal Basin," in *Fractals in the Earth Sciences*, C. C. Barton and P. R. La Pointe, Eds., Springer, Boston, MA, USA, 1995.

[13] G. M. Yu, H. P. Xie, J. F. Zhao, and L. Yang, "Fractal evolution of a crack network in overburden rock strata," *Discrete Dynamics in Nature and Society*, vol. 5, pp. 47–52, 1999.

[14] F. J. Molz, H. Rajaram, and S. Lu, "Stochastic fractal-based models of heterogeneity in subsurface hydrology: origins, applications, limitations, and future research questions," *Reviews of Geophysics*, vol. 42, no. 1, 2004.

[15] M. Qian and X. Miu, "Theoretical analysis on the structural form and stability of overlying strata in longwall mining," *Chinese Journal of Rock Mechanics and Engineering*, vol. 14, no. 2, pp. 97–106, 1995.

[16] Z. G. Wang, H. W. Zhou, and H. P. Xie, "Research on fractal characterization of mined crack network evolution in overburden rock stratum under deep mining," *Rock and Soil Mechanics*, vol. 30, pp. 2403–2408, 2009.

[17] A. Jafari and T. Babadagli, "Estimation of equivalent fracture network permeability using fractal and statistical network properties," *Journal of Petroleum Science and Engineering*, vol. 92, pp. 110–123, 2012.

[18] X. J. Wei, M. Z. Gao, Y. C. Lv, X. C. Shi, H. L. Gao, and H. W. Zhou, "Evolution of a mining induced fracture network in the overburden strata of an inclined coal seam," *International Journal of Mining Science and Technology*, vol. 22, no. 6, pp. 779–783, 2012.

[19] A. Jafari and T. Babadagli, "Relationship between percolation–fractal properties and permeability of 2-D fracture networks," *International Journal of Rock Mechanics and Mining Sciences*, vol. 60, pp. 353–362, 2013.

[20] H. Y. Li, W. H. Wang, Q. X. Qi, and L. Zhang, "Study on fissure development rule of overlying strata influenced by mining based on fractal theory," *Journal of China Coal Society*, vol. 39, pp. 1023–1030, 2014.

[21] H. U. Yaoqing, Y. Zhao, and D. Yang, "Simulation theory and method of 3D solid-liquid coupling," *Journal of Liaoning Technical University*, vol. 26, no. 2, pp. 204–206, 2007.

[22] Y. Zhao, *Multi Field Coupling of Porous Media and its Engineering Response*, Science Press, Beijing, China, 2010.

[23] X. Li, Y. Lu, Y. Kang, and B. Rao, *Experimental Simulation Technology of Rock Mechanics*, Science Press, Beijing, China, 2007.

[24] S. Li, Y. Zhou, L. Li, and Q. Zhang, "Development and application of a new similar material for underground engineering fluid-solid coupling model test," *Chinese Journal of Rock Mechanics and Engineering*, vol. 37, no. 6, pp. 1128–1137, 2012.